Time invariance of three-dimensional morphology of equiaxed dendrite: A phase-field study

Ryo Yamada[a], Mikihiro Kudo[b], Geunwoo Kim[b], Tomohiro Takaki[c], Yasushi Shibuta[d], Munekazu Ohno[a,*]

[a] *Division of Materials Science and Engineering, Faculty of Engineering, Hokkaido University, Kita 13 Nishi 8, Kita-ku, Sapporo, Hokkaido 060-8628, Japan*
[b] *Graduate School of Engineering, Hokkaido University, Kita 13 Nishi 8, Kita-ku, Sapporo, Hokkaido 060-8628, Japan*
[c] *Faculty of Mechanical Engineering, Kyoto Institute of Technology, Matsugasaki, Sakyo-ku, Kyoto 606-8585, Japan*
[d] *Department of Materials Engineering, The University of Tokyo, 7-3-1 Hongo, Bunkyo-ku, Tokyo 113-8656, Japan*

* Corresponding author: mohno@eng.hokudai.ac.jp

Abstract

Dendrite morphology has a significant effect on solute segregation and fluid flow in bulk metallic materials. Therefore, the detailed morphological evolution of dendrites is important to better understand these processes. Recently, three-dimensional (3D) dendrite morphology has been analyzed using interface shape distribution (ISD) maps that are spanned by the curvedness and shape factor of the local solid–liquid interface in an Al–Cu alloy. Data were collected through in-situ observations using synchrotron radiation imaging techniques [J.W. Gibbs et al.: *Sci. Rep*., **5** (2015) 11824]. This methodology is quite effective for describing 3D dendrites. In this study, we thoroughly investigated the morphological evolution and the related ISD map of free-growing equiaxed dendrites in an Al–3mass%Cu alloy using a quantitative phase-field model. The ISD was found to differ depending on the degree of undercooling. Importantly, the results indicate the presence of a time-invariant feature after sufficient branching and growth of secondary arms, when the degree of undercooling is substantial enough to produce a bunch of branching. The time invariance is considered a universal feature of equiaxed dendrite growth.

Keywords: solidification, equiaxed dendrite, phase-field model, time invariance

1. Introduction

Dendrites are formed during casting processes, and their morphology strongly affects the various physical properties of materials [1]. The dendrite morphology has been characterized by the primary dendrite arm spacing (or PDAS) and secondary dendrite arm spacing (or SDAS), which can be easily obtained from solidified microstructures, but are not always sufficient predictors of key macroscopic fluid dynamics properties. For instance, permeability, which has been broadly employed to predict macrosegregation, cannot be reliably reproduced from knowledge of only PDAS and SDAS [2]. Thus, further detailed information about the morphology, such as the solid–liquid interface area, is crucial for accurately predicting the permeability [3, 4]. Furthermore, Ohno et al. have highlighted the importance of

a detailed description of the dendrite morphology to predict microsegregation [5]. Therefore, it is important to properly characterize and clarify the detailed morphology of dendrites.

In-situ observation is an effective approach to obtain detailed information on growing dendrites. Recently, the use of synchrotron radiation imaging techniques with image-processing techniques, such as a time-interlaced model-based iterative reconstruction (TIMBIR) methodology, has facilitated the observation of the growth processes of three-dimensional (3D) dendrites in bulk metallic materials [6]. Using this new observation technique, Gibbs et al. characterized the 3D dendrite morphology in an Al–Cu alloy in terms of the shape factor and the curvedness of the local solid–liquid interface in dendrites; in addition, they plotted an interface shape distribution (ISD) map of the results [7]. The ISD map provides the existing probability or frequency of a given local morphology of the interface in terms of the shape factor and curvedness. Hence, the ISD map represents the statistical nature of the local interface morphology in the 3D dendrites. Gibbs et al. investigated the growth morphology and the related ISD map for free-growing dendrites under continuous cooling conditions. Their analysis of the ISD map demonstrated that the morphology of the dendrite is not self-similar with the distance from the tip. Further investigation should be aimed at clarifying the ISD map under different cooling conditions, such as isothermal holding under multiple undercooling conditions, as well as the details of the time dependence of the ISD map.

Computer simulation is an effective approach for investigating the 3D morphology of growing dendrites in metallic materials. In general, the free-growing dendrites can be well investigated in computer simulations because the effects of the mold wall (computational domain boundary) and other dendrites on it can readily and explicitly be excluded or included in the analysis. In this study, therefore, the time evolutions of free-growing 3D dendrites during the isothermal solidification of an Al–Cu alloy and the related ISD maps were investigated using the quantitative phase-field model [8-11] (hereinafter QPFM), which is one of the most effective and reliable approaches to describe the microstructural evolution processes in alloy systems. Our particular focus is on the effects of the degree of undercooling on these processes. The remainder of this paper is organized as follows. First, Section 2 briefly describes the theoretical background of QPFM, a method of dendrite morphology analysis, and the computational conditions of the analysis. Section 3 presents the calculated dendrites with various degrees of undercooling and analyzes the morphologies in terms of the shape factor and curvedness. Finally, Section 4 summarizes the results and new findings obtained herein.

2. Method

2.1. Quantitative phase-field model

A phase-field model (PFM) has been widely used to simulate the solidification of metallic alloy systems. A complex microstructure can be simulated using a PFM without tracking the moving interfaces, where the interface between the solid and liquid phases is described by a continuous variation in the phase-field variable that uses constant values assigned to each phase. However, the simulated results obtained from a conventional PFM depend on the interface thickness [8-11]. The QPFM was developed to overcome this issue, where the solution of the free-boundary problem is recovered in the thin-interface limit. This study used the QPFM developed by Ohno and Matsuura [10] and applied the calculation procedure described previously [12].

In the QPFM, the phase-field variable ϕ takes +1 in the solid phase, −1 in the liquid phase, and varies from +1 to −1 within the solid–liquid interface. The time evolution equation of ϕ is given by [8, 10]:

$$\tau_0[1+(1-k)u]a_s(\boldsymbol{n})^2\frac{\partial\phi}{\partial t} = W_0^2\nabla\cdot[a_s(\boldsymbol{n})^2\nabla\phi] + W_0^2\sum_{r=x,y,z}\frac{\partial}{\partial r}\left[|\nabla\phi^2|a_s(\boldsymbol{n})\frac{\partial a_s(\boldsymbol{n})}{\partial\left(\frac{\partial\phi}{\partial r}\right)}\right] + \phi(1-\phi^2) - \lambda(1-\phi^2)^2u \quad , \tag{1}$$

where τ_0 is the phase-field relaxation time, k is the equilibrium partition coefficient, u is the dimensionless local supersaturation, $a_s(\boldsymbol{n})$ is defined as shown in Eq. (2) below [13, 14], and t is the time. τ_0 is defined as $\tau_0 = a_2\lambda W_0^2/D_L$, where $a_2 = 0.6267$, λ is a coupling constant, W_0 is the interface thickness, and D_L is the solute diffusivity in the liquid phase. λ is given as $\lambda = a_1W_0/d_0$ where $a_1 = 0.8839$ and d_0 is the capillary length.

$$a_s(\boldsymbol{n}) = 1+\varepsilon_1\left(Q-\frac{3}{5}\right)+\varepsilon_2\left(3Q+66S-\frac{17}{7}\right) \quad , \tag{2}$$

where $\boldsymbol{n}$ is a unit vector pointing to the crystal orientation; ε_1 and ε_2 are the anisotropy parameters; $Q = n_x^4+n_y^4+n_z^4$; $S = n_x^2n_y^2n_z^2$; and n_i are the Cartesian components of $\boldsymbol{n}$. Furthermore, u is defined as $u \equiv (c_L-c_L^e)/(c_L^e-c_S^e)$, where c_L and c_S are the liquid and solid concentrations, respectively, and c_L^e and c_S^e are the equilibrium values. The time evolution of u is given by

$$\frac{1+k-(1-k)\phi}{2}\frac{\partial u}{\partial t} = \nabla\cdot\left[D_Lq(\phi)\nabla u+\frac{1}{2\sqrt{2}}\left(1-k\frac{D_S}{D_L}\right)W_0\{1+(1-k)u\}\frac{\partial\phi}{\partial t}\frac{\nabla\phi}{|\nabla\phi|}\right] + \frac{1}{2}[1+(1-k)u]\frac{\partial\phi}{\partial t} \quad , \tag{3}$$

where D_S is the solute diffusivity in the solid phase, and $q(\phi)$ is defined as

$$q(\phi) = \frac{1}{2}\left[(1+\phi)k\frac{D_S}{D_L}+1-\phi\right] \quad . \tag{4}$$

The inverse of d_0 is given by

$$\frac{1}{d_0} = \frac{RT_m(1-k)(c_L^e-c_S^e)}{v_m\gamma_0} \quad , \tag{5}$$

where R is the gas constant, T_m is the melting temperature of the pure solvent, v_m is the molar volume, and γ_0 is the average interfacial energy of the solid–liquid interface. The anisotropy of the interfacial

energy is incorporated through ε_1 and ε_2 (ε_2 is set to zero in this study). Furthermore, as noted in Ref. [12], although some of the present authors have recently proposed a variational formulation of a QPFM, wherein the cross-coupling terms of ϕ and u are derived naturally [11], the QPFM developed by Ohno and Matsuura [10] was employed herein to balance the computational cost with the numerical accuracy. To solve Eqs. (1) and (3) effectively and simultaneously, preconditioning [15] was employed.

2.2. Computational conditions

Eqs. (1) and (3) are discretized using a second-order finite difference scheme, and time integration is performed using the first-order Euler scheme. To simulate the morphological evolution of free-growing dendrites in Al–3mass%Cu under isothermal conditions, an initial solid seed was placed at the origin of the system occupied by the liquid phase. To reduce the computational cost, only one-eighth of the system was considered because of the four-fold symmetry of the interfacial energy anisotropy. The zero-flux boundary (or mirror boundary) condition is employed on the x-y, y-z, and z-x planes at $z = L_s$ ($z = 0$), $x = L_s$ ($x = 0$), and $y = L_s$ ($y = 0$), respectively, where L_s is the system size. We considered three different degrees of undercooling, $u_0 = -0.2$, -0.3, and -0.4, which correspond to $\Delta T = 1.6$, 2.8, and 4.2 K, respectively. The simulations were performed in a computational domain of 512^3 grid points with a grid spacing $dx = dy = dz = 0.65 \times 10^{-6}$, 0.50×10^{-6}, and 0.35×10^{-6} m for $u_0 = -0.2$, -0.3, and -0.4, respectively. The ratio of grid spacing to interface thickness (dx/W_0) was set to 1.2. These values were chosen to strike a balance between the accuracy and computational costs of a preliminary study that investigated the effects of domain size and grid spacing on the time evolution of free-growing dendrites. It was confirmed that these calculation conditions ensure that interface thickness are much smaller than the minimum curvature radius of dendrite tip in [100] direction. Note that the grid spacing decreases with a large $|u_0|$ because the dendrite morphology becomes finer with increased undercooling. The physical parameters used in the calculations are listed in Table 1. All the computations for dendritic growth were accelerated using multiple graphics processing units.

2.3. Characterization of morphology

The morphology of dendrites is characterized by the curvedness, *C* (also called "curvature" in Ref. [7]), and shape factor, *S,* of the local interface in a manner similar to that employed by Gibbs et al. [7]. These factors are defined and expressed as [16]:

$$C = \sqrt{\frac{\kappa_1^2 + \kappa_2^2}{2}} \tag{6}$$

and

$$S = \frac{2}{\pi} \tan^{-1} \frac{\kappa_2 + \kappa_1}{\kappa_2 - \kappa_1} , \tag{7}$$

where κ_1 and κ_2 are the maximum and minimum curvatures of the local interface, respectively. The relationship between these quantities and the morphology of the local interface is shown in Fig. 1. The

interface with $S = \pm 1, \pm 0.5$, and 0 corresponds to spherical, cylindrical, and saddle point shapes, respectively, and the sign of S specifies the convex direction of the interface. C denotes the degree to which the interface is curved.

The principal curvatures κ_1 and κ_2 are related to the average curvature H $(= (\kappa_2 + \kappa_1)/2)$ and the Gaussian curvature G $(= \kappa_2\kappa_1)$. In this study, H and G were computed as [17]:

$$H = \frac{1}{2|\nabla\varphi|^3}\left[\varphi_x^2\left(\varphi_{yy} + \varphi_{zz}\right) + \varphi_y^2(\varphi_{xx} + \varphi_{zz}) + \varphi_z^2\left(\varphi_{xx} + \varphi_{yy}\right) - 2\varphi_{yz}\varphi_y\varphi_z - 2\varphi_{xz}\varphi_x\varphi_z - 2\varphi_{xy}\varphi_x\varphi_y\right] \tag{8}$$

and

$$G = \frac{1}{|\nabla\varphi|^4}\left[\varphi_x^2\left(\varphi_{yy}\varphi_{zz} - \varphi_{yz}^2\right) + \varphi_y^2(\varphi_{xx}\varphi_{zz} - \varphi_{xz}^2) + \varphi_z^2\left(\varphi_{xx}\varphi_{yy} - \varphi_{xy}^2\right) - 2\varphi_x\varphi_y\left(\varphi_{xy}\varphi_{zz} - \varphi_{xz}\varphi_{yz}\right) - 2\varphi_x\varphi_z\left(\varphi_{xz}\varphi_{yy} - \varphi_{xy}\varphi_{yz}\right) - 2\varphi_y\varphi_z\left(\varphi_{yz}\varphi_{xx} - \varphi_{xy}\varphi_{xz}\right)\right] , \tag{9}$$

where $\varphi = \sqrt{2}W_0 \log\left(\frac{1-\phi}{1+\phi}\right)$ and φ_{ij} represents the partial derivative of φ in terms of i- and j-axes.

3. Results and Discussion

The time evolutions of the free-growing dendrites calculated for $u_0 = -0.2$, -0.3, and -0.4 are shown in Fig. 2. Branching occurs under all conditions, and branches become much finer as $|u_0|$ increases (i.e., as the undercooling increases). Note that dendrite morphology is generally affected by heat transfer, fluid flow, and interactions with other dendrites and/or mold walls. The study of dendrite morphology growing without any of the above effects provides a basis for understanding dendrite structures growing under various conditions.

The free-growing dendrites shown in Fig. 2 were quantitatively analyzed in detail using the local shape factor S, curvedness C, and the ISD map. Figure 3 shows the result for $u_0 = -0.2$, where local interfaces in 3D dendrites are colored according to the values of S and C in (a) and (b), respectively, and the ISD map is shown in (c). Here, (a-1) to (a-3) and (b-1) to (b-3) are magnified accordingly, and C in the ISD map is normalized by the average value of C at each time step, $\langle C \rangle$. The temporal change in $\langle C \rangle$ can be found in the Supplemental data. The reason for this normalization is explained later in this paper. In Figs. 3 (a) and (b), the tips of primary and secondary arms always exhibit a spherical shape ($S \approx 1.0$) with high curvedness. Note that the trunk of the primary arms and the root of secondary arms have a cylindrical shape of $S \approx -0.5$, while the edge of the secondary arms has $S \approx +0.5$ (see Fig. 3 (a-4)). In the ISD map of Fig. 3 (c), the probabilities at $S \approx -0.5$ and 0.5 increase with time. This suggests that a large portion of the interface has cylindrical shapes in this equiaxed dendrite. In addition, the probabilities of small $C/\langle C \rangle$ ($\approx$ 0.1-0.2) increase with time. This is ascribed to the increase in the flat surface area in the secondary dendrite arms (Fig. 3 (b-4)), which is known as a flattening of secondary dendrite arms and is consistent with past experiments [7]. This flattening is caused by interactions with the neighboring secondary

dendrite arms. Note that the interfaces with high curvedness can be found at both the edges and roots of the dendrite arms.

The results for $u_0 = -0.3$ and -0.4 are shown in Figs. 4 and 5, respectively. Similar features of the 3D dendrite morphology observed for $u_0 = -0.2$ (Figs. 3 (a) and (b)) can be seen in these cases as well. In Figs. 4 and 5, however, the dendrites grow not only in the preferential growth direction (i.e., <100>) but also in other growth directions, such as <111> and <110>, at the initial stage of evolution (Figs. 4 (a-2, b-2) and 5 (a-2, b-2)). This is due to the large degree of undercooling. The dendrite growing in the <111> direction can be observed even in the late stage for $u_0 = -0.4$ (Figs. 5 (a-4, b-4)). Also, the large undercooling causes the growth of the tertiary dendrite arms from the sides of the secondary dendrite arms (Figs. 4 (b-4) and 5 (b-4)). Namely, frequency of branching is very high in cases of $u_0 = -0.3$ and -0.4. This high frequency of branching decreases the existing probability at $S \approx -0.5$ because each arm mainly consists of interfaces with a positive value of S. Therefore, it results in a relatively small peak at $S \approx -0.5$ compared to $S \approx 0.5$ for $u_0 = -0.4$ (see Fig. 5 (c)).

The time evolutions of the ISD maps were also investigated in detail. The ISD maps for $u_0 = -0.3$ from $t = 0.4\ t_{\max}$ to $t = t_{\max}$, where $t_{\max}$ is 0.5 seconds (the maximum time of simulation), are shown in Fig. 6. The most important finding is that there is no significant change in the ISD maps after $t = 0.6\ t_{\max}$. Note that the dendrite grows substantially from $t = 0.6\ t_{\max}$ to $t = t_{\max}$. For instance, the total volume of the solid increases by more than double from $0.6\ t_{\max}$ to $t_{\max}$. Notwithstanding, the ISD map for free-growing dendrites becomes time-invariant at the late stage of growth (or after sufficient branching and growth of secondary arms). The same time-invariant behavior is found for $u_0 = -0.4$, whereas a slight change in the ISD map is observed for $u_0 = -0.2$. (Details of the results are provided in the Supplemental data). It is expected that the time invariance should appear even for $u_0 = -0.2$ when the calculation is carried out for a longer time in the larger computational system. These results indicate that the ISD map exhibits time-invariant features after sufficient branching and growth of the secondary arms in free-growing dendrites. This means that the dominant interface shape and its relative size do not change with time for free-growing dendrites for any degree of undercooling considered here. The existence of time invariance was quantitatively checked by calculating $\Delta P(C,S) = P(C,S) - \langle P(C,S) \rangle$, where $P(C,S)$ is the probability in the ISD map and $\langle P(C,S) \rangle$ is the time-averaged probability after $t = 0.6\ t_{\max}$. We found that the standard deviation of $\Delta P(C,S)$ takes less than 0.1 in the almost entire time range for $u_0 = -0.3$ and -0.4, which indicates the time invariance of ISD maps. The details can be found in Supplemental data.

It is important to note that the time invariance of ISD maps cannot be observed when the y-axis is set to C. In this case, the ISD maps clearly changed with time. This is because that C decreases as the size of microstructure increases with time. Time invariance appears only when C is normalized to $\langle C \rangle$. As mentioned in the introduction, the time invariance was not observed in the previous experimental work of ISD map [7]. This should be because the ISD map was obtained for continuous cooling condition in the experimental work [7], while the ISD maps in this work are calculated for isothermal solidification. This point will be investigated in a future work.

The probability distributions at $C/\langle C \rangle = 1.0$ on the ISD maps for different degrees of undercooling are compared in Fig. 7. The results are shown for different volume fractions of solids ($f_v = 0.23$, 0.68, and 1.14 %). The peaks of probability distributions appear at $S \approx -0.5$ and 0.5 in all cases. However, the peak height at $S \approx -0.5$ is significantly decreased when the degree of supercooling $|u_0|$ is large. The same

behavior was also observed for different values of $C/\langle C\rangle$ values (see Supplemental data). As described above, the decrease in the peak height originates from the high frequency of branching due to the large degree of undercooling. These results indicate that the detailed differences between dendrites growing under different cooling conditions can be expressed in the ISD map.

4. Conclusion

The morphological evolution of free-growing dendrites in an Al–3 mass% Cu alloy was studied using a QPFM. The dendrites calculated for different degrees of undercooling were analyzed in terms of curvedness, *C*, and shape factor, *S*, of the local interface, and the temporal changes of the probability distribution for the local curvedness and shape factors were investigated. The details of the dendrite morphology are well characterized in the ISD map. It was found that the peaks of probability appear at $S \approx \pm 0.5$ for all cases, indicating that the dendrites mainly consist of an interface with cylindrical shapes. Importantly, the ISD maps exhibit time-invariant behavior for a large degree of undercooling when *C* is normalized by the average value at each time step $\langle C\rangle$. This finding suggests that the dominant interface shape and its relative size do not change with time for the free-growing dendrite.

Note that free-growing dendrites under different undercooling conditions were considered in this work. In reality, a variety of factors affect the growth morphology, such as change in the temperature field, fluid flow, and interactions with other dendrites and/or mold walls. To advance our understanding, further research on these effects is required. The dendrite morphology growing under a constant cooling rate is currently under investigation, and the results will be reported soon. Furthermore,

Acknowledgements

This work was partially supported by KAKENHI, Grant-in-Aid for Scientific Research (B), No. 19H02486, from the Japan Society for the Promotion of Science (JSPS).

Availability of data

The data that support the findings of this study are available from the corresponding author upon reasonable request.

References

[1] W. Kurz and D. J. Fisher: *Trans Tech Publications*, **35** (1989) 316.
[2] Y. Natsume, D. Takahashi, K. Kawashima, E. Tanigawa, and K. Ohsasa, *Tetsu-to-Hagané*, **99** (2013) 2.
[3] T. Takaki, S. Sakane, M. Ohno, Y. Shibuta, and T. Aoki: *Acta Mater*., **164** (2019) 237.
[4] Y. Mitsuyama, T. Takaki, S. Sakane, Y. Shibuta, and M. Ohno: *Acta Mater*., **188** (2020) 282.
[5] M. Ohno, M. Yamashita, and K. Matsuura: *Int. J. Heat Mass Transf*., **132** (2019) 1004.

[6] K.A. Mohan, S.V. Venkatakrishnan, J.W. Gibbs, E.B. Gulsoy, X. Xiao, M. De Graef, P.W. Voorhees, and C.A. Bouman: *IEEE Transactions on Computational Imaging*, **1** (2015) 96-111.
[7] J.W. Gibbs, K.A. Mohan, E.B. Gulsoy, A.J. Shahani, X. Xiao, A. Bouman, M. De Greaf, and P.W. Voorhees: *Scientific Reports*, **5** (2015) 11824.
[8] A. Karma: *Phys. Rev. Lett*., **87** (2001) 115701.
[9] B. Echebarria, R. Folch, A. Karma, and M. Plapp: *Phys. Rev. E*, **70** (2004) 061604.
[10] M. Ohno and K. Matsuura: *Phys. Rev. E*, **79** (2009) 031603.
[11] M. Ohno, T. Takaki, and Y. Shibuta: *Phys. Rev. E*, **96** (2017) 033311.
[12] G. Kim, T. Takaki, Y. Shibuta, S. Sakane, K. Matsuura, and M. Ohno: *Comput. Mater. Sci*., **162** (2019) 76-81.
[13] S.K. Chan, H.H. Reimer, and K. Kahlweit: *J. Cryst. Growth*, 32 (1976) 303.
[14] W.R. Fehlner and S.H. Vosko: *Can. J. Phys*., 54 (1976) 2159.
[15] K. Glasner: *Journal of Comput. Phys*., **174** (2001) 695.
[16] J.J. Koenderink and A.J. van Doorn: *Image Vis. Comput*., 10 (1992) 557-564.
[17] J.W. Gibbs and P.W. Voorhees: *Integr. Mater. Manuf. Innov*., **3** (2014) 6.
[18] M. Gündüz and J.D. Hunt: *Acta metall*., 33 (1985) 1651-1672.
[19] T. Takaki, S. Sakene, M. Ohno, Y. Shibuta, T. Shimokawabe, and T. Aoki: *Acta Mater*., **118** (2016) 230.
[20] Y. Du, Y.A. Chang, B. Huang, W. Gong, Z. Jin, H. Xu, Z. Yuan, Y. Liu and Y. He, and F.-Y Xie: *Mater. Sci. Eng. A*, **363** (1989) 140.

Tables

Table 1. Physical parameters used in the present study.

Physical parameter	Value
Molar volume, v_m [m^3/mol]	1.0×10^{-6}
Average Interfacial energy, γ_0 [J/m^2]	0.15 [18]
Liquidus slope, m_L [K/mol.fraction]	–620 [19]
Melting temperature of pure Al, T_m [K]	933.25
Liquid diffusivity, D_L [m^2/sec]	3.0×10^{-9} [20]
Solid diffusivity, D_S [m^2/sec]	3.0×10^{-12} [20]
Equilibrium partition coefficient, k [-]	0.14 [19]
Anisotropy parameter, ε_1 [-]	0.08 [19]

Figures

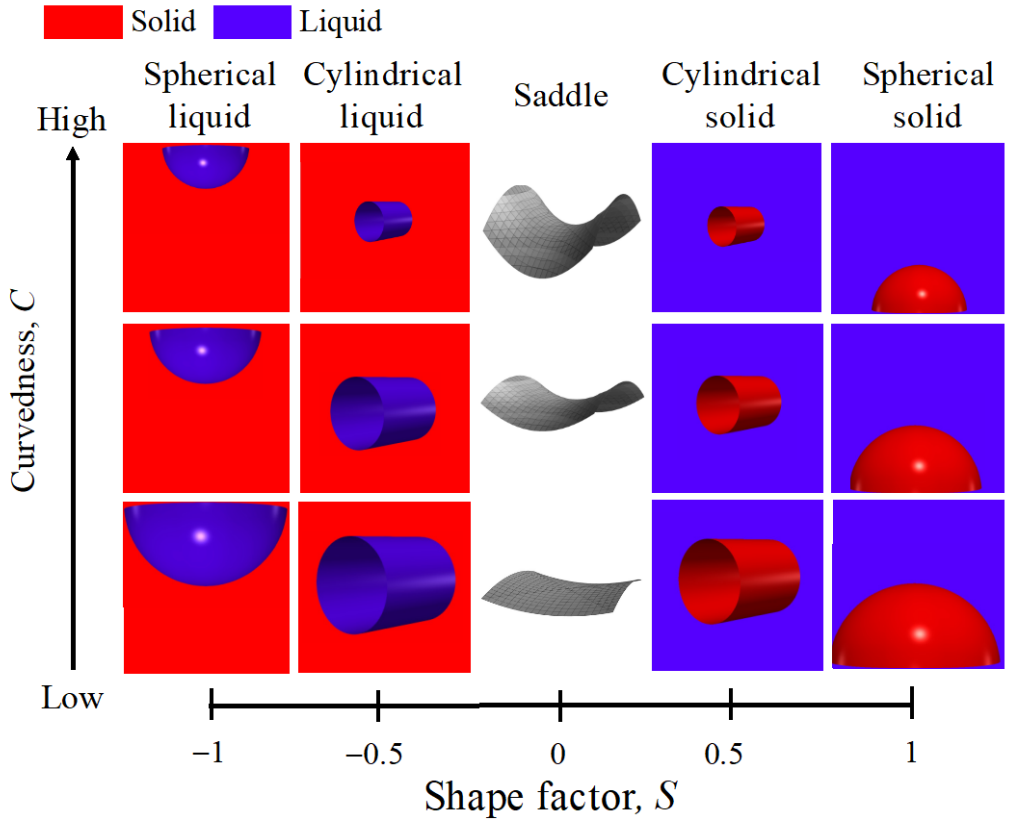

Fig. 1. Relation between morphology and shape factor and curvedness, where solid and liquid phases are shown in red and purple, respectively.

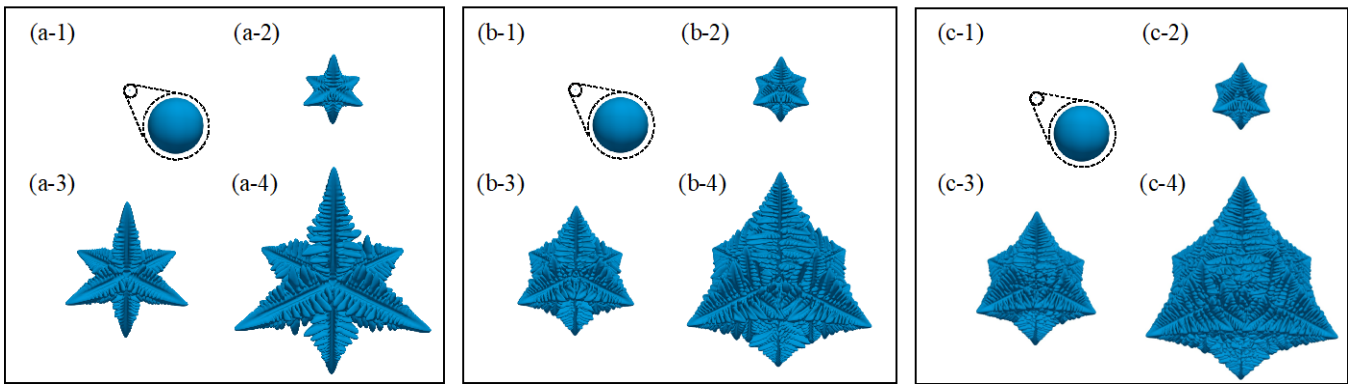

Fig. 2. Time evolutions of free-growing dendrites calculated for (a) $u_0 = -0.2$, (b) $u_0 = -0.3$, and (c) $u_0 = -0.4$. (a-1)/(b-1)/(c-1) to (a-4)/(b-4)/(c-4) are the snapshots at 0.0/0.0/0.0, 0.54/0.17/0.05, 1.07/0.33/0.10, and 1.61/0.50/0.14 seconds, respectively. The initial seeds of dendrite are magnified in (a-1), (b-1), and (c-1).

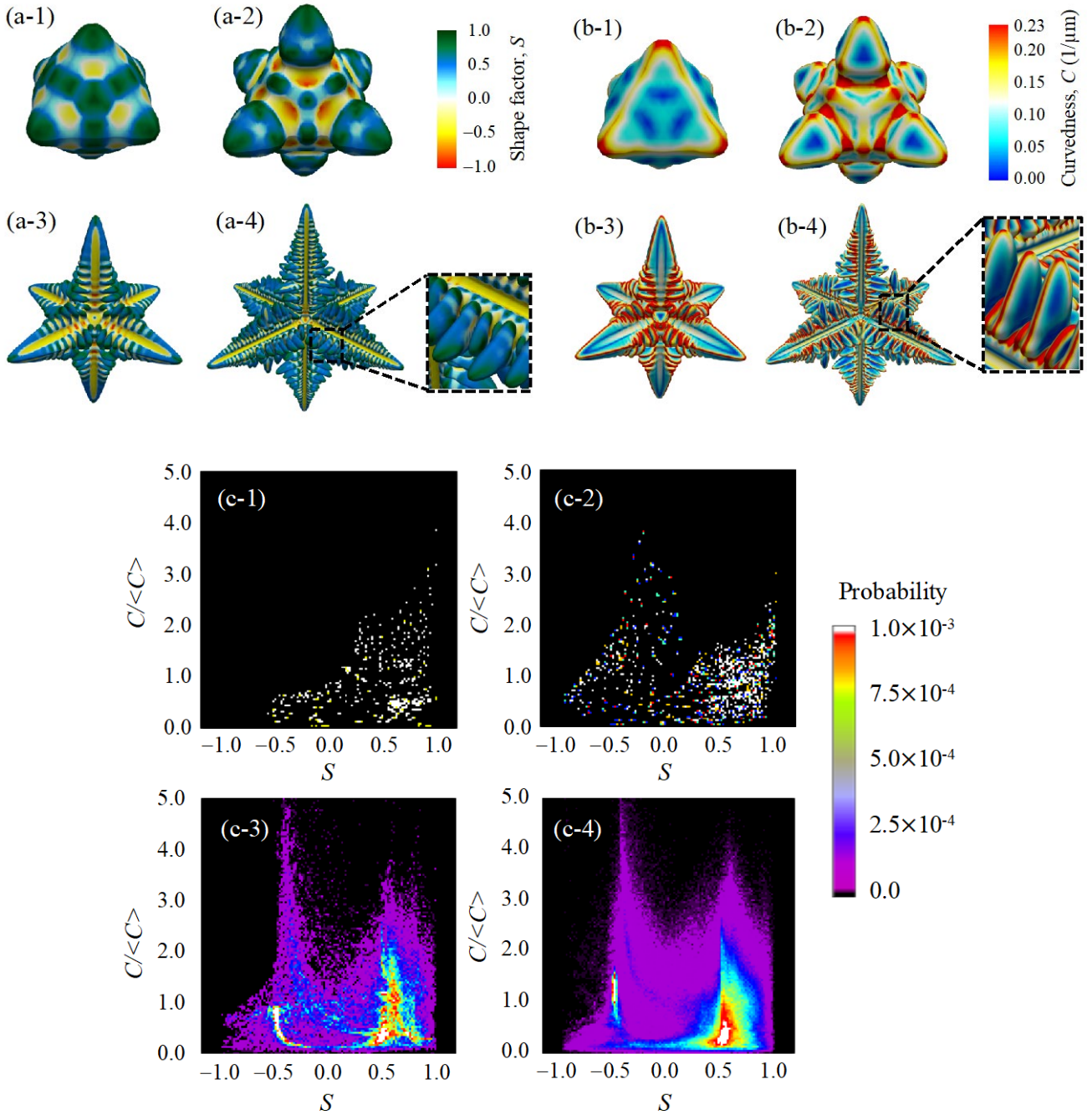

Fig. 3. Dendrite morphologies characterized by (a) shape factor and (b) curvedness with (c) the corresponding ISD maps for $u_0 = -0.2$ at (a-1, b-1, and c-1) 0.03, (a-2, b-2, and c-2) 0.09, (a-3, b-3, and c-3) 0.60, and (a-4, b-4, and c-4) 1.61 seconds. The morphologies shown in (a-1)-(a-3) and (b-1)-(b3) are magnified ones.

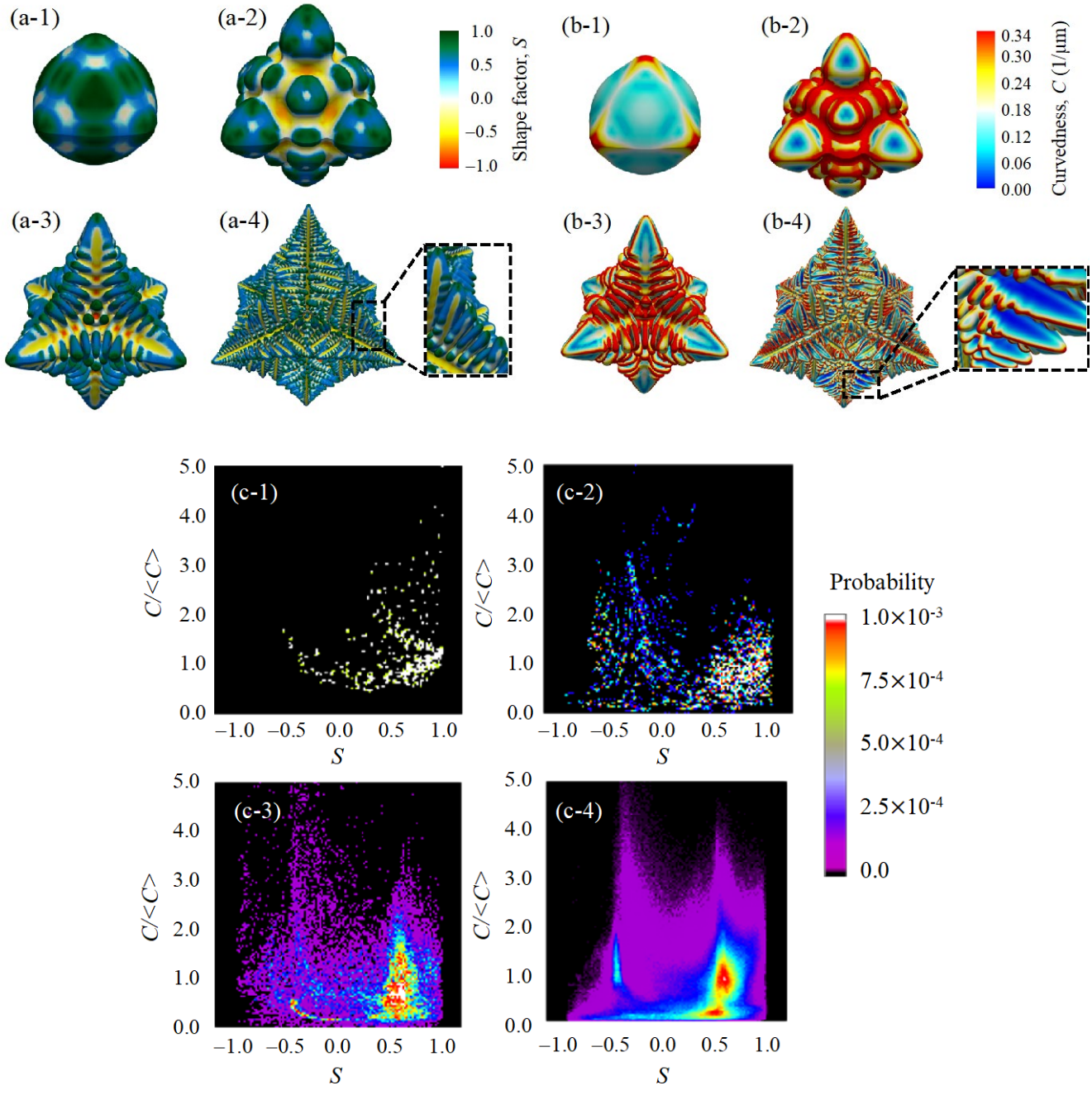

Fig. 4. Dendrite morphologies characterized by (a) shape factor and (b) curvedness with (c) the corresponding ISD maps for $u_0 = -0.3$ at (a-1, b-1, and c-1) 0.01, (a-2, b-2, and c-2) 0.02, (a-3, b-3, and c-3) 0.10, and (a-4, b-4, and c-4) 0.50 seconds. The morphologies shown in (a-1)-(a-3) and (b-1)-(b3) are magnified ones.

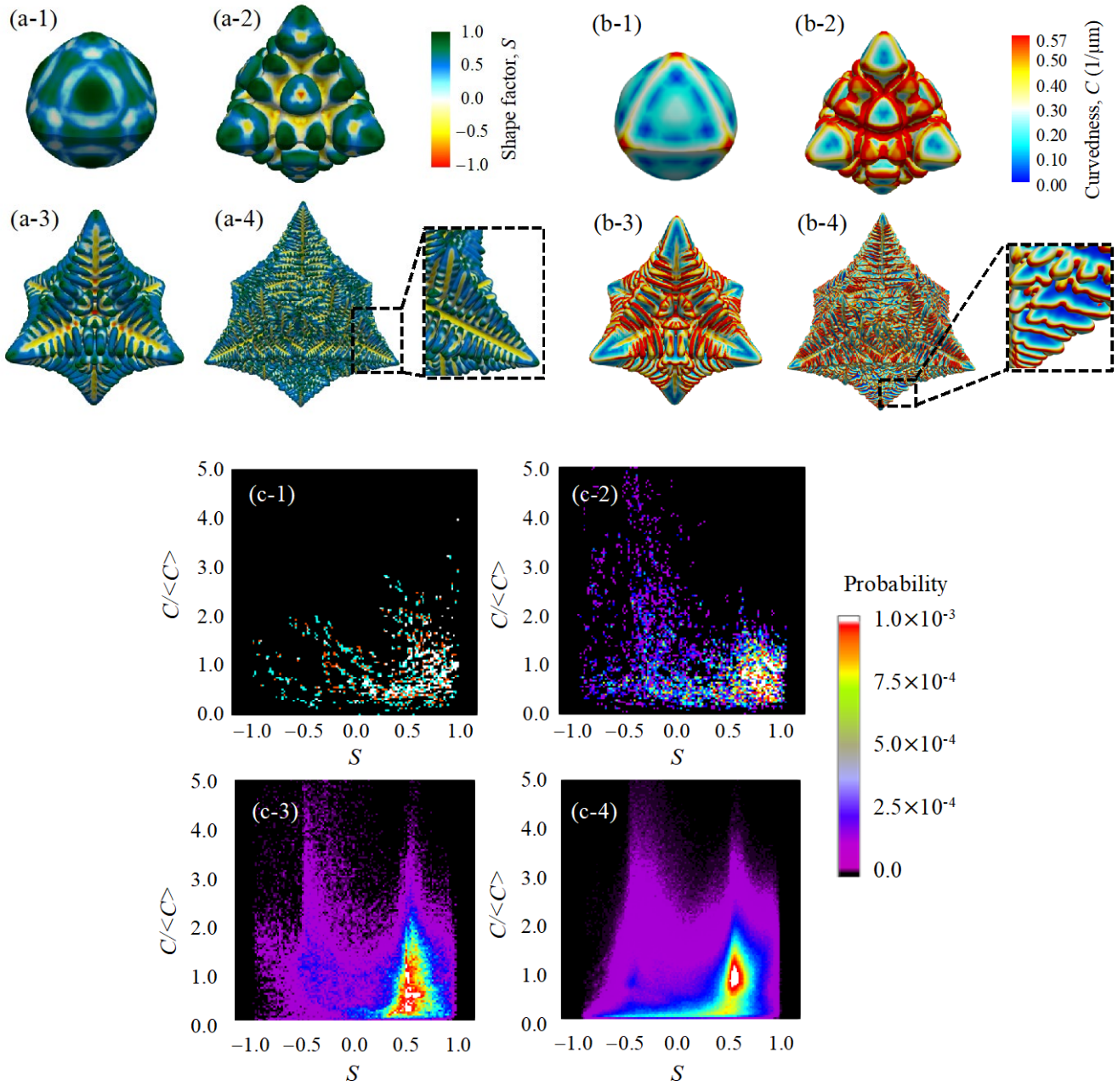

Fig. 5. Dendrite morphologies characterized by (a) shape factor and (b) curvedness with (c) the corresponding ISD maps for $u_0 = -0.4$ at (a-1, b-1, and c-1) 0.003, (a-2, b-2, and c-2) 0.01, (a-3, b-3, and c-3) 0.04, and (a-4, b-4, and c-4) 0.14 seconds. The morphologies shown in (a-1)-(a-3) and (b-1)-(b3) are magnified ones.

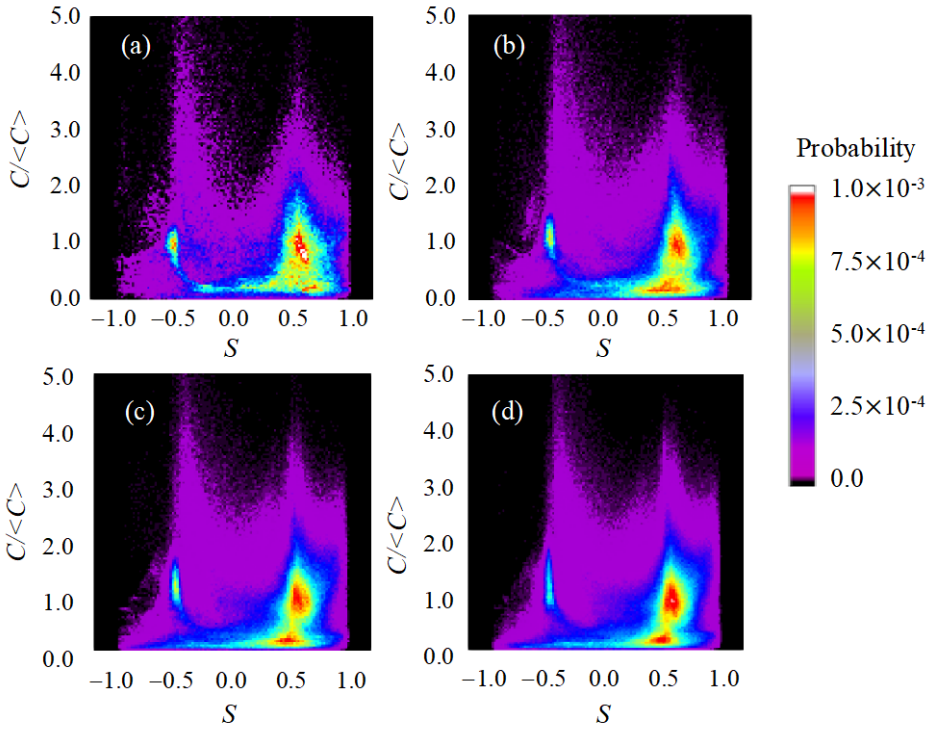

Fig. 6. Time evolution of ISD map for $u_0 = -0.3$ at (a) 0.4 $t_{\max}$, (b) 0.6 $t_{\max}$, (c) 0.8 $t_{\max}$, and (d) $t_{\max}$, where $t_{\max} = 0.50$ seconds.

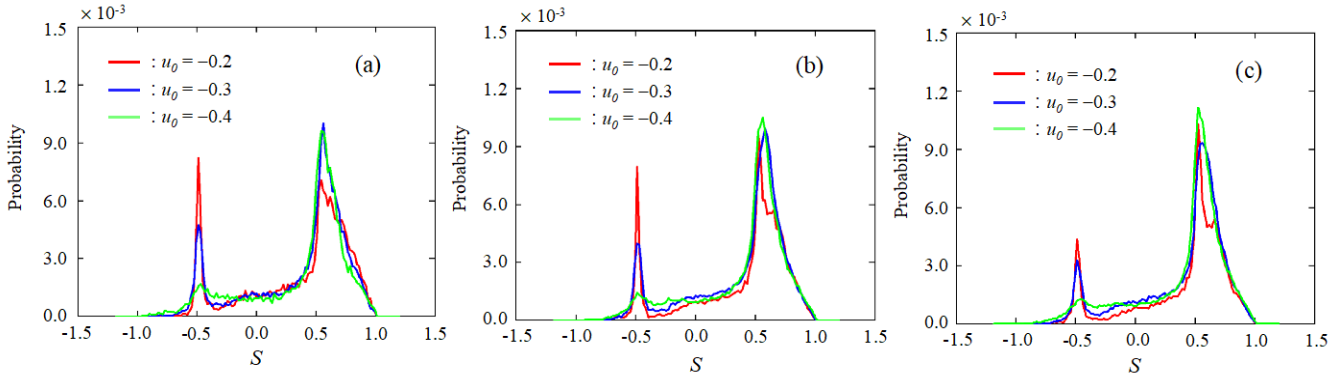

Fig. 7. Time evolution of probability distribution at $C/\langle C\rangle = 1.0$ at (a) f_v = 0.23, (b) f_v = 0.68, and (c) f_v = 1.14 %, where f_v is the volume fraction of solid. The red, blue, and green lines correspond to the results for $u_0 = -0.2$, –0.3, and –0.4, respectively.